Nonadiabatic Effects in Raman Spectra of $AlCl_4^-$-graphite Based Batteries

Dino Novko,[1,2] Qian Zhang,[3,4] and Payam Kaghazchi[5,*]

[1] *Center of Excellence for Advanced Materials and Sensing Devices, Institute of Physics, Bijenička 46, Zagreb, 10000 Croatia*

[2] *Donostia International Physics Center (DIPC), Paseo Manuel de Lardizabal 4, Donostia-San Sebastián, 20018 Spain*

[3] *State Key Laboratory Base of Eco-chemical Engineering, Qingdao University of Science and Technology, Qingdao, China*

[4] *College of Chemistry and Molecular Engineering, Qingdao University of Science and Technology, Qingdao, China*

[5] *Forschungszentrum Jülich GmbH, Institute of Energy and Climate Research (IEK-1), Materials Synthesis and Processing, Jülich, 52425, Germany*

(Received 4 April 2019; revised manuscript received 10 June 2019; published 8 August 2019)

Raman spectroscopy is one of the most valuable experimental techniques for quality assessment and structural characterization of sample materials. As such, it has been applied to understand the mechanism of the staging of anions and cations into graphite-based electrodes in a variety of energy storage devices such as Al batteries, dual-ion cells, and Li-ion batteries. However, the correlation between the Raman peaks and intercalation stages is still unclear in most of these systems. This is due to the fact that the modeling of electron-phonon coupling in highly doped graphite systems is beyond the standard Born-Oppenheimer approximation. Here, we simulate the Raman peaks for $AlCl_4^-$-intercalated graphite in Al batteries by using a nonadiabatic coupling theory. Specifically, we successfully correlate the Raman peaks of the *G* phonon in $AlCl_4^-$-doped graphite with experiment for intercalation stages 1, 2, and 4, while stage 3 appears to be absent. Stages 1 and 2 have not been observed in experimental XRD patterns. We therefore believe that the $AlCl_4^-$-graphite intercalation compound has a core-shell structure with a maximum stage of 4 or 3 in the core and 2 or 1 in the shell. In addition, the observed intense narrow Raman bands for the Al-ion battery cathode are due to the high level of graphite doping and are explained in terms of low electron-phonon decay rates.

DOI: 10.1103/PhysRevApplied.12.024016

I. INTRODUCTION

The dynamic interplay between electronic and ionic degrees of freedom can lead to the breakdown of the Born-Oppenheimer approximation in the theoretical description of material properties [1,2]. For instance, in the presence of excess electron or hole carriers a nonadiabatic (NA) effect can arise due to the proximity of electron excitation and vibrational energies. In that case, the phonon spectrum can be drastically altered due to NA coupling [3]. This phenomenon has been observed by means of Raman spectroscopy in, for example, carbon-based materials, including graphite intercalation compounds (GICs) [4–7], graphene [8–10], nanotubes [11,12], and boron-doped diamond [13]. A theoretical first-principles description based on time-dependent perturbation theory [3,8] was proven to be quite accurate for correlating the electron or hole doping concentration with observed phonon frequency shifts due to NA coupling. This method has been successfully employed to determine the doping concentration, Fermi-energy shifts, and intercalation stages in some GIC systems (e.g., $FeCl_3$-GIC) by tracking the frequency changes of the Raman-active *G* phonon [5,6,14].

An interesting system where clear frequency shifts of the *G* phonon are expected is $AlCl_4^-$-graphite, which is formed by intercalation of $AlCl_4^-$ into a graphite cathode during the charging process of aluminum-ion batteries (AIBs). The AIB, with its high charge and discharge rate (75C) and calendar life (over 7000 cycles at room temperature), is a promising energy storage device [15–17]. A conventional Al-ion battery consists of an Al metal anode, a graphitic-foam cathode, and an Al_xCl_y-containing nonflammable ionic-liquid electrolyte. The battery operates through the electrochemical deposition and dissolution of Al at the anode and intercalation and deintercalation of

*p.kaghazchi@fz-juelich.de

$AlCl_4^-$ anions in the cathode. Raman measurements and x-ray diffraction (XRD) measurements have been carried out to characterize the mechanism of $AlCl_4^-$-graphite staging behavior. Although several theoretical studies have been devoted to calculating $AlCl_4^-$ diffusion in graphite as well as the atomic structure, XRD pattern, and potential profile of $AlCl_4^-$-graphite [18–20], no study has been reported of the simulation of the corresponding Raman spectrum. Such a study, based on NA theory, can provide valuable information on the doping concentration and the staging mechanism of intercalation during charge and discharge of AIBs. In this paper, by using density-functional theory (DFT) calculations including nonadiabatic coupling effects, we calculate the Raman G-band peak positions for $AlCl_4^-$-GIC. By comparing the calculated values with the previously reported experimental data at different levels of intercalation, we characterize the staging mechanism of $AlCl_4^-$ intercalation into graphite.

II. RESULTS AND DISCUSSION

Within many-body perturbation theory, the NA phonon frequency of the Raman G band (ω_G) can be obtained from the following equation [3,4,8,13]:

$$\omega_G^2 = (\omega_G^0)^2 - 2\omega_G^0 \,\mathrm{Re}\,\pi_G(\omega_G), \tag{1}$$

where ω_G^0 is the adiabatic phonon frequency and $\mathrm{Re}\,\pi_G$ is the real part of the complex phonon self-energy due to the electron-phonon interaction π_G. Its imaginary part is related to the phonon linewidth (FWHM) and the intensity of the corresponding peak, i.e., $\gamma_G = -2\,\mathrm{Im}\,\pi_G(\omega_G)$ and $I_G \propto 1/\gamma_G$. In cases where only the first-order electron-phonon coupling is considered (i.e., the G phonon excites pure noninteracting electron-hole pairs), π_G is defined as

$$\pi_G(\omega) = \sum_{\mu\mu'\mathbf{k}} \frac{\omega \left| g_G^{\mu\mu'}(\mathbf{k}) \right|^2}{\varepsilon_{\mu'\mathbf{k}} - \varepsilon_{\mu\mathbf{k}}} \frac{f(\varepsilon_{\mu\mathbf{k}}) - f(\varepsilon_{\mu'\mathbf{k}})}{\omega + \varepsilon_{\mu\mathbf{k}} - \varepsilon_{\mu'\mathbf{k}} + i\eta}, \tag{2}$$

where $\varepsilon_{\mu\mathbf{k}}$, μ, and $\mathbf{k}$ are the electron energy, band index, and momentum vector, respectively. η is an infinitesimal parameter (i.e., $\eta \to 0^+$, which ensures energy conservation in the electron-phonon-coupling process). $f(\varepsilon_{\mu\mathbf{k}}) = 1/(e^{(\varepsilon_{\mu\mathbf{k}}-\varepsilon_F)/k_BT}+1)$ is the Fermi-Dirac distribution function, where ε_F is the Fermi energy, T is the temperature, and k_B is the Boltzmann constant. The function that quantifies the strength of the coupling between electrons and the G-band phonon is $g_G^{\mu\mu'}(\mathbf{k})$. When the vertical transitions between different electronic bands (i.e., $\mu \neq \mu'$) are suppressed (as is the case for highly doped graphite or graphene, where $\omega_G \ll \varepsilon_{\mu\mathbf{k}} - \varepsilon_{\mu'\mathbf{k}}$), the frequency shift (i.e., $\Delta\omega_G \equiv \omega_G - \omega_G^0$) as obtained from Eq. (1) can be approximated as $\Delta\omega_G \approx N(\varepsilon_F)\left\langle |g_G|^2 \right\rangle_{\varepsilon_F}$ [4], where $N(\varepsilon_F)$ is the electronic density of states (DOS) at the Fermi energy and $\left\langle |g_G|^2 \right\rangle_{\varepsilon_F}$ is the squared average of $g_G^{\mu\mu'}(\mathbf{k})$ over the Fermi surface. From this, it is obvious that a higher DOS gives larger shifts.

When a strong electron-phonon coupling dominates the Raman spectrum, the phonon linewidths should be estimated by use of a higher-order electron-phonon-coupling theory (i.e., where the G phonon excites electron-hole pairs, which in turn scatter on other phonons in the system) [4,21,22]. When such processes are active, the phonon linewidth of the G phonon is $\gamma_G^{\text{e-ph}} \propto 1/(\tau_{e\text{-ph}}\omega_G)$, where $1/\tau_{e\text{-ph}}$ is the electron-phonon scattering rate. The latter can

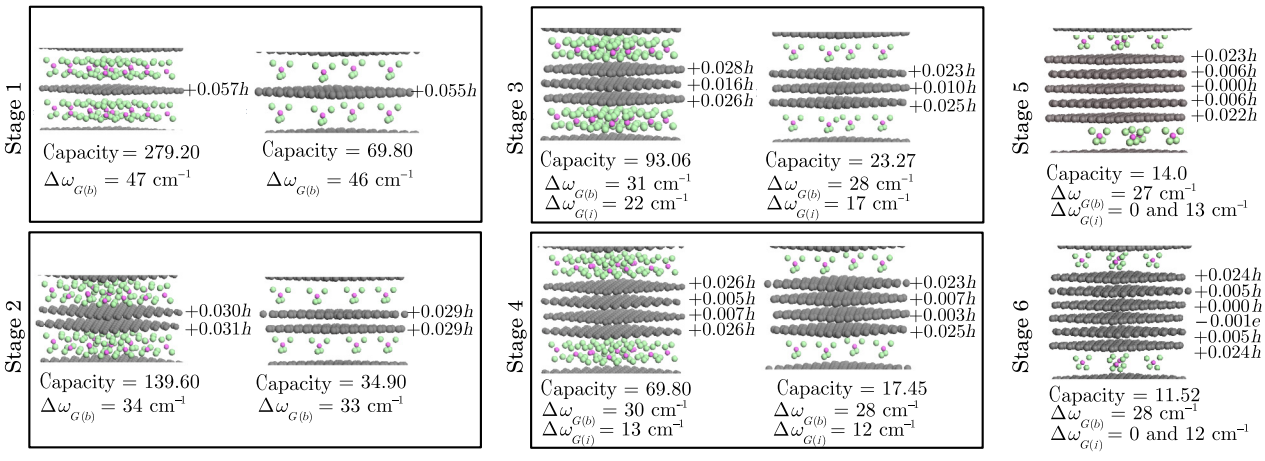

FIG. 1. Side views of calculated structures, with Bader charges (number of positive charges per graphene unit cell, i.e., per two carbon atoms) and estimated capacity (in mA h/g), for various stages (n = 1–6) of $AlCl_4^-$-GIC. The corresponding frequency shifts of the G-band phonon in the i- and b-layers obtained from NA theory are also shown.

TABLE I. Average values of p charge per graphite layer unit cell (i.e., per two carbon atoms) for various intercalation stages of $AlCl_4^-$-doped graphite extracted from Bader-charge analysis, the corresponding Fermi energies ε_F of the graphite layers, and the frequency shifts of the G-band phonon $\Delta\omega_G$ obtained from the NA theory. The results are shown for both a low (L) and a high (H) concentration of $AlCl_4^-$ molecules in the intercalation layer, as shown in Fig. 1. The experimental frequency shifts are shown for comparison [15,17]. The experimental frequency of the G-band phonon in pure graphite is 1584 cm^{-1}, as reported in Ref. [15,17]. Our theoretical result is 1587 cm^{-1}. In addition, we show the intercalation (↑) and deintercalation (↓) voltages corresponding to the experimental frequency shifts obtained in Ref. [17].

	4		3			
Stage	i-layer	b-layer	i-layer	b-layer	2	1
p charge L	0.005	0.024	0.01	0.024	0.029	0.055
p charge H	0.006	0.026	0.016	0.027	0.030	0.057
$-\varepsilon_F$ (eV)	0.4	0.6	0.5	0.6	0.7	1.1
$\Delta\omega_G$ L (cm^{-1})	12	28	17	28	33	46
$\Delta\omega_G$ H (cm^{-1})	13	30	22	31	34	47
$\Delta\omega_G^{exp.}$ (cm^{-1}) [15]	3	24	⋯		⋯	52
$\Delta\omega_G^{exp.}$ (cm^{-1}) [17]	6–7	25–28	⋯		35	47–48
↑ voltage (V) [17]	1.94		⋯		2.1	2.3
↓ voltage (V) [17]	1.5		⋯		1.66	2.01

be calculated as the following [22,23]:

$$1/\tau_{e\text{-ph}} = \frac{2\pi}{\omega_G}\int_0^{\omega_G} d\omega'(\omega_G - \omega')\alpha^2F(\omega'). \qquad (3)$$

The Eliashberg spectral function $\alpha^2F(\omega')$ contains information about which phonon modes of the system scatter with electrons and with what intensity.

Figure 1 (see also Table I) illustrates the results of a Bader-charge analysis for various intercalation stages of $AlCl_4^-$-doped graphite, where the final numbers represent the average positive charge per graphene unit cell, i.e., per two carbon atoms. $AlCl_4^-$ is an electron acceptor, which means that it takes negative charges from the graphite layers and leaves behind positively charged holes. Stages 1 and 2 are characterized by a single charged graphite layer (the so-called bounding layer or b-layer), which is in contact with the intercalated $AlCl_4^-$ [24]. On the other hand, stages 3 and 4 contain an additional type of graphite layer (the so-called interior layer or i-layer), which is not in contact with $AlCl_4^-$ [24]. Consequently, it is expected that Raman spectroscopy will reveal only one peak for stages 1 and 2, but two separated peaks for stages 3 and 4. Higher stages, i.e., 5 and 6, are characterized by three differently charged layers (one b-layer and two different i-layers). As a result, these stages should give three distinguishable Raman peaks. Also, we obtain very similar doping of the graphite layer for low and high concentrations of $AlCl_4^-$ anions (1 and 4 molecules per 4×4 unit cell, respectively). Nevertheless, for various intercalation stages we get quite different doping. In fact, the number of holes per graphene unit cell for stage 1 is twice as large as that for stage 2. Note that the Bader charge per single carbon site varies within each of the compound layers presented in Fig. 1. For example, the difference between the maximum and minimum values of the charge per carbon atom is $0.011h$ for stage 1. However, in Raman spectroscopy the long-wavelength source probes many carbon sites. For this reason, we consider the average positive charge per graphene unit cell.

Afterwards, we use the DFT-calculated average positive charges (p) of the graphite layers per unit cell of the $AlCl_4^-$-GIC to evaluate the adiabatic phonon frequencies of the G phonon ω_G^0 and solve Eqs. (1) and (2) to obtain the NA phonon frequencies ω_G. Note that in this step the latter equations are evaluated for a single graphite layer doped with the average p charge as obtained from the above Bader-charge analyses of $AlCl_4^-$-GIC. The result for pure (undoped) graphene is $\omega_G = 1587$ cm^{-1}, which is in good agreement with the experimental value of 1584 cm^{-1} [15, 17]. The frequency shift (with respect to $\omega_G = 1587$ cm^{-1}) as a function of excess p doping is shown in Fig. 2(a). There are two contributions to this frequency shift. The first one is due to the p-charge-induced compression of the equilibrium lattice size. This effect leads to a larger value of the phonon frequency [8,25] (orange diamonds). The second effect is due to the electron-phonon coupling, which also increases with the level of p doping. This effect causes significant NA corrections, which were calculated by use of Eqs. (1) and (2) [4,8,9] (the blue diamonds include both of the contributions). In fact, the second contribution is slightly more pronounced than the first. For example, when the excess p charge is 0.06 per unit cell, the shift arising from the first effect is $\Delta\omega_G^0 \approx 16$ cm^{-1}, while the total shift including both effects is $\Delta\omega_G \approx 48$ cm^{-1} [compare the blue and orange diamonds in Fig. 2(a)]. The increase due to the NA effect can be understood by considering $N(\varepsilon_F)$ as a function of p doping [Fig. 2(b)]. When the p-charge concentration is increased, the Fermi level moves from the

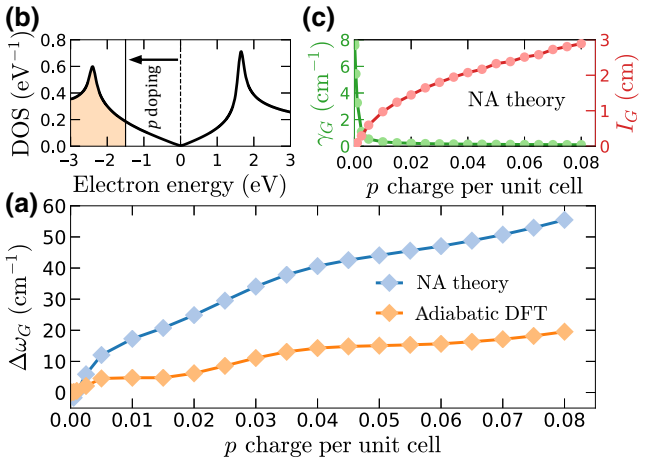

FIG. 2. (a) Frequency shift of the G-band phonon $\Delta\omega_G$ as a function of the excess positive charge density per unit cell. The blue diamonds show results obtained from the NA theory and by considering the expansion of the equilibrium lattice parameters due to the excess positive charge. The orange diamonds show the results obtained by considering only the latter effect. (b) Electronic density of states for graphene. (c) G-phonon linewidth γ_G (green) and the corresponding Raman intensity I_G (red) due to NA effects as a function of the excess positive charge density per unit cell.

Dirac point to lower energies, as a result of which the value of $N(\varepsilon_F)$ increases considerably, which then results in a larger $\Delta\omega_G$.

The calculated G-phonon shifts $\Delta\omega_G$ for the average Bader charge of the C atoms in each graphene sheet for different stages and concentrations are listed in Fig. 1 and Table I. Hereafter, unless mentioned otherwise, we mainly compare our calculations with the experimental results for $AlCl_4^-$-GICs in Al-ion batteries presented in Refs. [15,17]. For stages 1 and 2, we have a large frequency shift, which is in good agreement with the experimental results for a high level of charging state, i.e., high voltages of 2.3 and 2.1 V, respectively (increasing voltages) [15,17]. By comparing the simulated $\Delta\omega_G$ for stages 3 and 4 with the experimental results, we find that the Raman spectrum for 1.94 V (increasing voltage) is due to stage 4, while it seems that stage 3 is absent in the experiment. The results for the b-layer in stage 4 are in excellent agreement with the experiments, while the frequency shifts for the corresponding i-layer are slightly higher than that extracted from the experiments. This discrepancy might arise from the uncertainty in the Bader charge analysis, but also from the fact that the experimental Raman signal of this lower peak is quite weak. The absence of stage 3 was also reported for an $AlCl_3$-GIC in an analysis of observed Raman spectra and XRD pattern data [24,26]. However, note that the process of intercalation in the $AlCl_3$-GIC was performed in vacuum using the two-zone vapor transport method, and it thus differs from the electrochemical process of $AlCl_4^-$ intercalation into graphite in Al-ion batteries [15,17].

Our simulated Raman peaks for $AlCl_4^-$-GIC in stages 5 and 6 (shown in Fig. 1) have three different peaks, assigned to an undoped i-layer, a slightly doped i-layer, and a b-layer. These three peaks have not been discussed in experimental measurements for $AlCl_4^-$-GIC [15,17]. However, experimental Raman spectra of a few-layer $FeCl_3$-GIC obtained by a vapor transport method reveal multiple (≥ 3) G peaks associated with differently charged graphite layers [6,27].

The reported experimental frequency shifts of $\Delta\omega_G = 47$ and 52 cm^{-1} at the full intercalation stage in $AlCl_4^-$-doped graphite are the largest among graphite intercalation compounds with p-type donors, i.e., hole-doped graphite (see Ref. [24] for a comparison). This indicates that the Fermi energy in this compound can reach quite a low value. This is confirmed by our theoretical calculations, which estimate it to go down to around -1.1 eV for a p charge per unit cell of 0.057, which is even lower than the value reported in $FeCl_3$-doped graphite [6,24]. The calculated value of $\Delta\omega_G = 47$ cm^{-1} is in excellent agreement with the experimental values.

To summarize the results for the frequency shift of the G mode, in Fig. 3 we show the corresponding experimental results as a function of intercalation voltage as obtained in Ref. [17] and schematically depict the accompanying intercalation stages as obtained from our NA calculations.

Another interesting feature observed in the experiments is that the intensity of the Raman signal for the graphite layer with the higher doping concentration is larger than that for the lower doping concentration [15,17]. By calculating the NA G-phonon linewidths for the i- and b-layers in stage 4 $AlCl_4^-$-GIC, we find that the ratio of the corresponding Raman-peak intensities is $I_{G(b)}/I_{G(i)} = 2.8$ [see Fig. 2(c)]. Also, we find that the intensities for stage 1

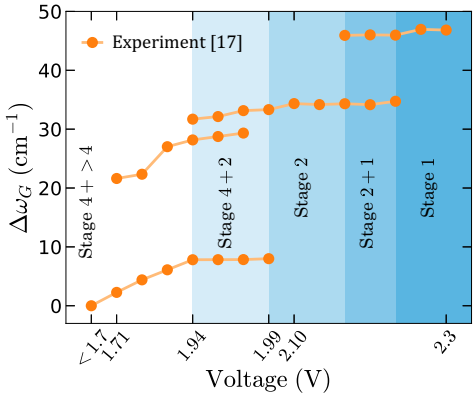

FIG. 3. Experimental frequency shifts of the G-phonon mode as a function of intercalation voltage as reported in Ref. [17]. The staging process obtained from the comparison of the NA-theory results and the experimental data is shown as well.

are higher than those for stage 4, i.e., $I^{s1}_{G(b)}/I^{s4}_{G(b)} = 1.5$ and $I^{s1}_{G(b)}/I^{s4}_{G(i)} = 4.2$. This effect is due to suppression of the G-phonon-induced electron excitations for higher dopings [8], which in turn results in lower phonon linewidths and, thus, in larger intensities. Nevertheless, the calculated intensity ratios are only qualitatively in agreement with the experimental data in Refs. [15,17]. This is because, apart from the first-order electron-phonon effect, there are other significant contributions to the phonon linewidth and intensity in the observed Raman spectra such as higher-order electron-phonon interactions [4,21,22,28] and inhomogeneities [10,29]. It is well established that the G-phonon linewidth and the Raman intensity broadens and decreases substantially with increasing concentration of alkali metal atoms [10,24,30]. In fact, in the final (stage 1) intercalation phase the G band acquires a broad and asymmetric Breit-Wigner-Fano line shape, which is often attributed to interference between the phonon and the electronic continuum [10,24,31]. Conversely, the Raman spectrum for the final stage of the $AlCl_4^-$-GIC displays a narrow and intense peak (i.e., a symmetric Lorentzian shape) for the G phonon. In Refs. [4,10], the source of the large phonon linewidths (and small intensities) in an alkali-doped GIC was mainly attributed to higher-order electron-phonon interactions. In that case, the phonon linewidth is highly sensitive to the electron-phonon scattering rate $1/\tau_{e\text{-ph}}$, as discussed above. By employing the methodology developed in Refs. [22,23,28], we get $1/\tau_{e\text{-ph}} \approx 116$ meV for stage 1 Li-GIC (n charge = 0.57 and $\varepsilon_F = 1.6$ eV) and $1/\tau_{e\text{-ph}} \approx 31$ meV for stage 1 $AlCl_4^-$-GIC (p charge = 0.057 and $\varepsilon_F = -1.1$ eV). Considering also that $\omega_G(\text{Li}) < \omega_G(AlCl_4^-)$, this estimation implies, in agreement with the experiments, that the G-phonon linewidth and intensity coming from higher-order electron-phonon interactions in $AlCl_4^-$-GIC are significantly narrower and higher, respectively, than in Li-GIC. Note that the Raman phonon linewidth and intensity might also be affected by disorder and anharmonic effects. Further quantitative analysis of the narrow and broad structures in Raman spectra of highly p- and n-doped GICs is of great interest [31]. However, this goes beyond the scope of the present work.

In addition, we discuss the correlation between the real part of the optical conductivity $\mathrm{Re}\,\sigma(\omega)$ and the Raman signal. Qualitatively, the phonon linewidth is connected to the optical conductivity by $\gamma \propto \omega\,\mathrm{Re}\,\sigma(\omega)$ [21]. This suggests that the narrow and intense feature observed for the G phonon in $AlCl_4^-$-GIC reflects a very small optical conductivity at ω_G, $\mathrm{Re}\,\sigma(\omega_G)$. Further, due to high doping concentration in the stage 1 intercalation phase, $AlCl_4^-$-GIC could also have a high direct current (dc) conductivity $\sigma(0) \equiv \sigma_{\mathrm{dc}}$ (note that $\sigma_{\mathrm{dc}} \propto$ charge concentration). Finally, from the intensity of the Raman G peak and the significant doping concentration we conclude that the corresponding ratio of the dc and optical conductivities $\sigma_{\mathrm{dc}}/\sigma_{\mathrm{opt}}$, which is a figure of merit for highly conductive materials, might be significant for $AlCl_4^-$-GIC. Such a desirable feature has been observed, for example, in $FeCl_3$-GIC [27] and Li-GIC [32].

III. CONCLUSION

In summary, by using DFT calculations that include nonadiabatic coupling effects, we have calculated the peak position and analyzed the linewidth and intensity of Raman G bands for $AlCl_4^-$-graphite compounds in Al-ion batteries. It is found that $AlCl_4^-$-intercalation-induced p doping of graphite leads to a blueshift of the G band. The increase in the frequency is due to the hole-induced contraction of C—C bonds as well as electron-phonon coupling, with the latter effect being larger. At the low stages 1 and 2, where all graphene sheets are in contact with $AlCl_4^-$ molecules, single G bands at 1633 and 1620 cm^{-1}, respectively, are obtained. At the higher stages 3 and 4, a high and a low G band related to bounding and interior graphene sheets, respectively, are computed. Although the high band is at the same position for both stages (1615 cm^{-1}), the low band for stage 4 is at 1599 cm^{-1}, which is 5 cm^{-1} smaller than that for stage 3. For the higher staging numbers of 5 and 6, three peaks are expected. Two peaks are at almost the same positions as for stage 4. The third peak is at 1587 cm^{-1}, which is the band position for bare graphite. This peak is related to graphene sheets which are far from the $AlCl_4^-$ molecules. The peak positions for stages 1, 2, and 4 are very close to the experimental Raman data for GICs in Al-ion batteries. However, the measured XRD data indicate that stages 1 and 2 are not formed. Thus, we propose that at the end of charging, $AlCl_4^-$-GICs have core-shell structures with stage 4 in the core and stage 1 or 2 in the shell region.

ACKNOWLEDGMENTS

D.N. gratefully acknowledges financial support from the European Regional Development Fund for the Center of Excellence for Advanced Materials and Sensing Devices (Grant No. KK.01.1.1.01.0001). Financial support from the Donostia International Physics Center (DIPC) during various stages of this work is also highly acknowledged. Computational resources were provided by the DIPC computing center. Q. Z. and P.K. gratefully acknowledge supports from the "China Scholarship Council" (CSC) and "Bundesministerium für Bildung und Forschung" (BMBF). Q. Z and P.K. also acknowledge the North-German Supercomputing Alliance (HLRN) for providing HPC resources.

APPENDIX: COMPUTATIONAL DETAILS

The DFT-based NA frequency shifts presented in Table I are obtained as follows. First, we compute the fully relaxed ground state of the compounds presented in Fig. 1 (i.e.,

stages 1–6 of $AlCl_4^-$-graphite). From these calculations we extract the average Bader charge of each layer in the supercell. Afterwards, we use the computed average Bader charges (per original unit cell of the graphite layer, i.e., per two carbon atoms) to calculate the accompanying compressions of the unit cell constants [8]. Finally, we compute Eqs. (1) and (2) for the corresponding single graphite layers with these average Bader charges.

To model $AlCl_4^-$-graphite, we focus on stages 1–6 (Rüdorff model) and use a 4×4 unit cell (two carbon atoms per 1×1 unit cell of a graphene sheet) with one $AlCl_4^-$ anion (referred to as "low concentration"). In addition, we consider four $AlCl_4^-$ anions in the 4×4 unit cell for stages 1–4 (referred to as "high concentration"). The capacity is calculated as $(Fn_{AlCl_4^-})/(3.6n_C m_C)$, where F and m_C are the Faraday constant and the molar mass of the C atom, respectively; $n_{AlCl_4^-}$ and n_C are the numbers of anions and carbon atoms, respectively, in the unit cell. The multiplier 3.6 in the denominator ensures that the value of the capacity is obtained in mA h/g instead of A s/g. The atomic structures and Bader charges are calculated using DFT calculations by the projector augmented-plane-wave code VASP [33]. The generalized gradient approximation exchange-correlation functional proposed by Perdew, Burke, and Ernzerhof [34] with the D3 dispersion correction proposed by Grimme [35,36] is applied. An energy cutoff value of 470 eV and $3 \times 3 \times 1$ k-point mesh sampling are used. Unit-cell and atomic-coordinate optimization are performed for all compounds until the maximum force acting on the atoms falls below 0.01 eV/Å.

Isolated p-doped graphite layers are then considered to compute adiabatic and nonadiabatic phonon frequencies within the DFT by using the plane-wave-based QUANTUM ESPRESSO (QE) package [37] with a plane-wave cutoff energy of 50 Ry. The average of the calculated Bader charges of the C atoms in each graphite layer (as obtained in VASP calculations) is considered to model each isolated p-doped graphite layer using a jellium model, where the excess charge is compensated by a uniform charged background. The core-electron interaction is approximated with ultrasoft pseudopotentials. The local-density approximation is used for the exchange and correlation functional. Phonon-related quantities (phonon adiabatic energies ω_G^0 and the electron-phonon function g^2) are obtained by means of density-functional perturbation theory [38], where a $(30 \times 30 \times 1)$ Monkhorst-Pack (MP) grid is used in order to achieve proper convergence of the adiabatic phonon spectra. The contraction of the graphite layer unit cell due to the presence of the external p charge is accounted for by using the results from Ref. [8]. The electron momentum summations in Eq. (2) are computed with a finer $(420 \times 420 \times 1)$ MP grid as implemented in QE, with a broadening of $\eta = 20$ meV. The electron and phonon momentum summations in the Eliashberg function α^2F, required to calculate the electron-phonon scattering rate in Eq. (3), are achieved on $(300 \times 300 \times 1)$ and $(30 \times 30 \times 1)$ MP grids, respectively. The broadening for the latter summations is 40 and 1.5 meV, respectively. More details regarding the summations of Eqs. (2) and (3) can be found in Refs. [22,28].

Note that NA coupling effects can also be obtained by directly computing Eqs. (1)–(3) for the structures depicted in Fig. 1. However, this approach is computationally quite demanding. Moreover, this model does not allow for contraction or expansion of C—C bonds in independent graphite layers with different concentrations of charge, which we believe is a realistic effect that might appear in these compounds. Therefore, isolated p-doped graphite layers are considered to be applicable to modeling our GIC structures, since graphite layers with different average charges experience different in-plane forces [8] but are held together only by weak van der Waals forces.

[1] E. G. Brovman, and Yu. Kagan, The phonon spectrum of metals, Sov. Phys. JETP **25**, 365 (1967).

[2] E. G. Maksimov, and S. V. Shulga, Nonadiabatic effects in optical phonon self-energy, Solid State Commun. **97**, 553 (1996).

[3] Feliciano Giustino, Electron-phonon interactions from first principles, Rev. Mod. Phys. **89**, 015003 (2017).

[4] A. Marco Saitta, Michele Lazzeri, Matteo Calandra, and Francesco Mauri, Giant Nonadiabatic Effects in Layer Metals: Raman Spectra of Intercalated Graphite Explained, Phys. Rev. Lett. **100**, 226401 (2008).

[5] Da Zhan, Li Sun, Zhen Hua Ni, Lei Liu, Xiao Feng Fan, Yingying Wang, Ting Yu, Yeng Ming Lam, Wei Huang, and Ze Xiang Shen, $FeCl_3$-based few-layer graphene intercalation compounds: Single linear dispersion electronic band structure and strong charge transfer doping, Adv. Funct. Mater. **20**, 3504 (2010).

[6] Weijie Zhao, Ping Heng Tan, Jian Liu, and Andrea C. Ferrari, Intercalation of few-layer graphite flakes with $FeCl_3$: Raman determination of fermi level, layer by layer decoupling, and stability, J. Am. Chem. Soc. **133**, 5941 (2011).

[7] Julio C. Chacón-Torres, Ludger Wirtz, and Thomas Pichler, Manifestation of charged and strained graphene layers in the raman response of graphite intercalation compounds, ACS Nano **7**, 9249 (2013).

[8] Michele Lazzeri, and Francesco Mauri, Nonadiabatic Kohn Anomaly in a Doped Graphene Monolayer, Phys. Rev. Lett. **97**, 266407 (2006).

[9] Simone Pisana, Michele Lazzeri, Cinzia Casiraghi, Kostya S. Novoselov, A. K. Geim, Andrea C. Ferrari, and Francesco Mauri, Breakdown of the adiabatic born – oppenheimer approximation in graphene, Nat. Mater. **6**, 198 (2007).

[10] C. A. Howard, M. P. M. Dean, and F. Withers, Phonons in potassium-doped graphene: The effects of electron-phonon

interactions, dimensionality, and adatom ordering, Phys. Rev. B **84**, 241404(R) (2011).
[11] Nicolas Caudal, A. Marco Saitta, Michele Lazzeri, and Francesco Mauri, Kohn anomalies and nonadiabaticity in doped carbon nanotubes, Phys. Rev. B **75**, 115423 (2007).
[12] Stefano Piscanec, Michele Lazzeri, J. Robertson, Andrea C. Ferrari, and Francesco Mauri, Optical phonons in carbon nanotubes: Kohn anomalies, peierls distortions, and dynamic effects, Phys. Rev. B **75**, 035427 (2007).
[13] Fabio Caruso, Moritz Hoesch, Philipp Achatz, Jorge Serrano, Michael Krisch, Etienne Bustarret, and Feliciano Giustino, Nonadiabatic Kohn Anomaly in Heavily Boron-doped Diamond, Phys. Rev. Lett. **119**, 017001 (2017).
[14] Francisco J. Bezares, Adolfo De Sanctis, J. R. M. Saavedra, Achim Woessner, Pablo Alonso-González, Iban Amenabar, Jianing Chen, Thomas H. Bointon, Siyuan Dai, Michael M. Fogler, D. N. Basov, Rainer Hillenbrand, Monica F. Craciun, F. Javier Garca de Abajo, Saverio Russo, and Frank H. L. Koppens, Intrinsic plasmon-phonon interactions in highly doped graphene: A near-field imaging study, Nano Lett. **17**, 5908 (2017).
[15] Meng-Chang Lin, Ming Gong, Bingan Lu, Yingpeng Wu, Di-Yan Wang, Mingyun Guan, Michael Angell, Changxin Chen, Jiang Yang, Bing-Joe Hwang, and Hongjie Dai, An ultrafast rechargeable aluminium-ion battery, Nature **520**, 324 (2015).
[16] Di-Yan Wang, Chuan-Yu Wei, Meng-Chang Lin, Chun-Jern Pan, Hung-Lung Chou, Hsin-An Chen, Ming Gong, Yingpeng Wu, Chunze Yuan, Michael Angell, Yu-Ju Hsieh, Yu-Hsun Chen, Cheng-Yen Wen, Chun-Wei Chen, Bing-Joe Hwang, Chia-Chun Chen, and Hongjie Dai, Advanced rechargeable aluminium ion battery with a high-quality natural graphite cathode, Nat. Commun. **8**, 14283 (2017).
[17] Michael Angell, Chun-Jern Pan, Youmin Rong, Chunze Yuan, Meng-Chang Lin, Bing-Joe Hwang, and Hongjie Dai, High coulombic efficiency aluminum-ion battery using an $AlCl_3$-urea ionic liquid analog electrolyte, Proc. Natl. Acad. Sci. **114**, 834 (2017).
[18] Preeti Bhauriyal, Arup Mahata, and Biswarup Pathak, The staging mechanism of $AlCl_4$ intercalation in a graphite electrode for analuminium-ion battery, Phys. Chem. Chem. Phys. **19**, 7980 (2017).
[19] Michael L. Agiorgousis, Yi-Yang Sun, and Shengbai Zhang, The role of ionic liquid electrolyte in an aluminum-graphite electrochemical cell, ACS Energy Lett. **2**, 689 (2017).
[20] Chun-Jern Pan, Chunze Yuan, Guanzhou Zhu, Qian Zhang, Chen-Jui Huang, Meng-Chang Lin, Michael Angell, Bing-Joe Hwang, Payam Kaghazchi, and Hongjie Dai, An operando x-ray diffraction study of chloroaluminate anion-graphite intercalation in aluminum batteries, Proc. Natl. Acad. Sci. **115**, 5670 (2018).
[21] E. Cappelluti, Electron-phonon effects on the raman spectrum in MgB_2, Phys. Rev. B **73**, 140505(R) (2006).
[22] Dino Novko, Nonadiabatic coupling effects in MgB_2 re-examined, Phys. Rev. B **98**, 041112(R) (2018).
[23] Dino Novko, Dopant-induced plasmon decay in graphene, Nano Lett. **17**, 6991 (2017).
[24] M. S. Dresselhaus, and G. Dresselhaus, Intercalation compounds of graphite, Adv. Phys. **51**, 1 (2002).
[25] L. Pietronero, and S. Strässler, Bond-length Change as a Tool to Determine Charge Transfer and Electron-phonon Coupling in Graphite Intercalation Compounds, Phys. Rev. Lett. **47**, 593 (1981).
[26] G. M. Gualberto, C. Underhill, S. Y. Leung, and G. Dresselhaus, Raman and infrared spectra of graphite-$AlCl_3$, Phys. Rev. B **21**, 862 (1980).
[27] Ivan Khrapach, Freddie Withers, Thomas H. Bointon, Dmitry K. Polyushkin, William L. Barnes, Saverio Russo, and Monica F. Craciun, Novel highly conductive and transparent graphene-based conductors, Adv. Mater. **24**, 2844 (2012).
[28] D. Novko, M. Alducin, and J. I. Juaristi, Electron-mediated Phonon-phonon Coupling Drives the Vibrational Relaxation of CO on Cu(100), Phys. Rev. Lett. **120**, 156804 (2018).
[29] Casiraghi Cinzia, Probing disorder and charged impurities in graphene by raman spectroscopy, Phys. Status Solidi Rapid Res. Lett. **3**, 175 (2009).
[30] J. C. Chacón-Torres, A. Y. Ganin, M. J. Rosseinsky, and T. Pichler, Raman response of stage-1 graphite intercalation compounds revisited, Phys. Rev. B **86**, 075406 (2012).
[31] Martin G. Hell, Niels Ehlen, Boris V. Senkovskiy, Eddwi H. Hasdeo, Alexander Fedorov, Daniela Dombrowski, Carsten Busse, Thomas Michely, Giovanni di Santo, Luca Petaccia, Riichiro Saito, and Alexander Grüneis, Resonance raman spectrum of doped epitaxial graphene at the lifshitz transition, Nano Lett. **18**, 6045 (2018).
[32] Wenzhong Bao, Jiayu Wan, Xiaogang Han, Xinghan Cai, Hongli Zhu, Dohun Kim, Dakang Ma, Yunlu Xu, Jeremy N. Munday, H. Dennis Drew, Michael S. Fuhrer, and Liangbing Hu, Approaching the limits of transparency and conductivity in graphitic materials through lithium intercalation, Nat. Commun. **5**, 4224 (2014).
[33] G. Kresse, and J. Furthmüller, Efficient iterative schemes for ab initio total-energy calculations using a plane-wave basis set, Phys. Rev. B **54**, 11169 (1996).
[34] John P. Perdew, Kieron Burke, and Matthias Ernzerhof, Generalized Gradient Approximation Made Simple, Phys. Rev. Lett. **77**, 3865 (1996).
[35] Stefan Grimme, Jens Antony, Stephan Ehrlich, and Helge Krieg, A consistent and accurate ab initio parametrization of density functional dispersion correction (DFT-D)for the 94 elements H-pu, J. Chem. Phys. **132**, 154104 (2010).
[36] Stefan Grimme, Stephan Ehrlich, and Lars Goerigk, Effect of the damping function in dispersion corrected density functional theory, J. Comput. Chem. **32**, 1456 (2011).
[37] Paolo Giannozzi, Stefano Baroni, Nicola Bonini, Matteo Calandra, Roberto Car, Carlo Cavazzoni, Davide Ceresoli, Guido L. Chiarotti, Matteo Cococcioni, Ismaila Dabo, *et al.*, Quantum espresso: a modular and open-source software project for quantum simulations of materials, J. Phys.: Condens. Matter **21**, 395502 (2009).
[38] Stefano Baroni, Stefano de Gironcoli, Andrea Dal Corso, and Paolo Giannozzi, Phonons and related crystal properties from density-functional perturbation theory, Rev. Mod. Phys. **73**, 515 (2001).